Chinese Chemical Letters 37 (2026) 111311

Contents lists available at ScienceDirect

Chinese Chemical Letters

journal homepage: www.elsevier.com/locate/cclet

Dynamic self-engineering of Fe-doped $NiSe_2$ into amorphous γ-$Fe_xNi_{1-x}OOH$ ultrathin nanosheets *via* electrochemical reconstruction for alkaline oxygen evolution

Elhussein Desoki Helal[a,b,1], Wenhai Xu[a,1], Liyao Gao[a], Yizhe Li[a], Hao Sun[a], Qingzhen Xu[a], Imran Ali Chandio[a], Safdar Abbas[a], Abdul Hameed Pato[a], Mohamed Mokhtar Mohamed[b], Man Zhao[a,*], Wen Liu[a,*]

[a] State Key Laboratory of Chemical Resource Engineering, College of Chemistry, Beijing University of Chemical Technology, Beijing 100029, China
[b] Chemistry Department, Faculty of Science, Benha University, Benha 13518, Egypt

ARTICLE INFO

Article history:
Received 26 February 2025
Revised 7 May 2025
Accepted 13 May 2025
Available online 13 May 2025

Keywords:
Oxygen evolution reaction
Water splitting
Iron-doped nickel selenide
Pre-catalyst
γ-$Fe_xNi_{1-x}OOH$

ABSTRACT

We report a facile low-temperature synthesis of Fe-doped $NiSe_2$ nanoparticles as an efficient pre-catalyst, which undergoes complete electrochemical reconstruction into amorphous γ-$Fe_xNi_{1-x}OOH$ nanosheets (<2 nm thickness) during activation process of cyclic voltammetry. The reconstituted catalyst achieves record-low overpotentials of 163 mV at 20 mA/cm^2 and 230 mV at 300 mA/cm^2, with a Tafel slope of 33.8 mV/dec and a turnover frequency (TOF) of 0.1 s^{-1} at overpotential of 210 mV. Remarkably, it shows outstanding operational stability with negligible activity decay after 300 h chronopotentiometry at 100 mA/cm^2. Through multimodal *ex situ*/*in situ* characterizations, we conclusively identify the *in situ*-formed amorphous γ-$Fe_xNi_{1-x}OOH$ nanosheets as the active phase, where Fe doping optimizes the electronic structure of Ni sites while the ultrathin morphology maximizes exposed active centers. This work establishes a universal precatalyst engineering strategy through controlled structural evolution of metastable precursors, applicable to diverse energy conversion systems.

© 2026 Published by Elsevier B.V. on behalf of Chinese Chemical Society and Institute of Materia Medica, Chinese Academy of Medical Sciences.

OER plays a pivotal role in sustainable energy conversion technologies such as water electrolysis and metal air batteries. However, its intrinsically sluggish kinetics, arising from the multi-step proton coupled electron transfer process ($4OH^- \rightarrow O_2 + 2H_2O + 4e^-$), necessitates highly efficient electrocatalysts to reduce overpotentials and enable practical applications. Although noble-metal oxides (*e.g.*, IrO_2 and RuO_2) are excellent OER electrocatalysts, their scarcity, prohibitive cost and poor stability have prompted ever-increasing efforts for seeking alternative non-precious-metal-based electrocatalysts [1–3].

Nickel-based non-oxidic materials have emerged as promising candidates for alkaline OER due to their surface reconstruction into oxyhydroxide phases (*e.g.*, γ-NiOOH) under operational conditions [4,5]. γ-NiOOH is a promising alkaline OER electrocatalyst, which has a large interplanar distance facilitating the movement of water (H_2O) and hydroxide (OH^-) ions through it, resulting in more exposed surface area and in turn high activity and stability [6]. The reconstructed phases of γ-NiOOH, whether forming core-shell surface structures or defect-rich bulk phases, consistently outperform their conventionally synthesized counterpart in OER activity [7,8]. Li *et al.* obtained NiSe@NiOOH core–shell hyacinth-like nanostructures *via in situ* electrochemical oxidation (ISEO), demonstrating OER activity with overpotential of 332 mV at 50 mA/cm^2 [9]. In another study, carbonate-intercalated γ-NiOOH particles were *in situ* derived from Ni sulfide under the alkaline OER conditions, achieving overpotential of 255 mV at 10 mA/cm^2 [10]. Other study showed that K-intercalated γ-NiOOH was *in situ* obtained from amorphous Nickel Pnictides during operation process of OER, achieving outstanding performance [11]. Recent advances further suggest that amorphous catalysts and ultrathin 2D nanostructures provide superior catalytic performance compared to crystalline or bulk materials, owing to their abundant defect sites and maximized surface accessibility [12,13]. Inspired by these findings, we aimed to design a Ni-based precatalyst capable of *in situ* transforming into amorphous ultrathin γ-NiOOH nanosheets during activation process, thereby synergistically integrating structural and compositional advantages for enhanced activity and stability.

* Corresponding authors.
E-mail addresses: zhaom@buct.edu.cn (M. Zhao), wenliu@buct.edu.cn (W. Liu).
[1] These authors contributed equally to this work.

https://doi.org/10.1016/j.cclet.2025.111311
1001-8417/© 2026 Published by Elsevier B.V. on behalf of Chinese Chemical Society and Institute of Materia Medica, Chinese Academy of Medical Sciences.

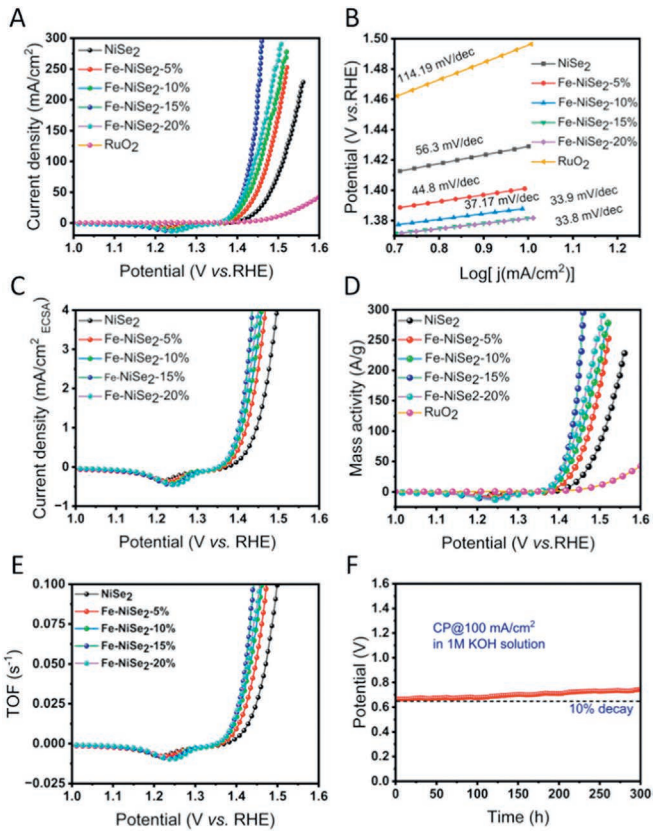


Fig. 1. Catalytic OER performances of the as-prepared samples and commercial RuO_2 in 1 mol/L aqueous KOH solution. (A) Polarization curves, (B) Tafel plots, (C) normalized polarization curves by ECSA, (D) mass activities, (E) TOF values, (F) chronopotentiometry (CP) test of Fe-$NiSe_2$-15 % at 100 mA/cm^2 for 300 h.

NiFe selenides have attracted particular interest due to their optimal electronic structure for OER intermediate adsorption. Despite their potential, conventional synthetic methods for NiFe selenides require high-temperatures (>400 °C), leading to polydisperse particles with mixed phase compositions and limited active site exposure, thus compromising catalytic performance [14,15]. Consequently, there is an urgent need for innovative synthesis that can produce phase-pure NiFe selenides with controlled nanostructures under mild conditions.

Herein, we demonstrate a rapid low-temperature synthesis of phase-pure Fe-doped $NiSe_2$ nanoparticles *via* a hydrazine hydrate assisted selenization strategy (Scheme S1 in Supporting information). By controlling the feeding ratio of $FeCl_3{\cdot}6H_2O$ into $NiCl_2$ precursors (denoted as x %, where x = 5, 10, 15, 20), a series of Fe-$NiSe_2$-x % catalysts (Table S1 in Supporting information) were obtained within 180 min at 80 °C. Comprehensive characterizations including X-ray diffraction (XRD), transmission electron microscopy (TEM), and energy-dispersive X-ray (EDX) mapping (Figs. S1-S4 in Supporting information) confirms the formation of homogeneous cubic $NiSe_2$ nanoparticles (20-50 nm in length) with uniform Fe doping and no detectable impurity phases.

The electrocatalytic performance of Fe-$NiSe_2$-x % catalysts (x = 5, 10, 15, 20), bare $NiSe_2$ and commercial RuO_2 was systematically evaluated for OER in 1 mol/L KOH using a three-electrode configuration. Prior to assessing the electrochemical activities, an activation process of 200 cyclic voltammetry (CV) cycles was conducted for the catalysts (Figs. S5 and S6 in Supporting information). Linear sweep voltammetry (LSV) curves after *iR*-correction (Fig. 1A, Figs. S7 and S8 in Supporting information) reveal a pronounced Fe-doping-dependent activity trend. The Fe-$NiSe_2$-15 % electrode delivers an ultralow overpotential (η) of 163 mV at 20 mA/cm^2, outperforming both RuO_2 (η = 307 mV) and other Fe-$NiSe_2$-x % variants (η = 218 mV for $NiSe_2$, 188 mV for 5 % Fe, 178 mV for 10 % Fe, and 165 mV for 20 % Fe) (Fig. S9A in Supporting information). This performance ranks among the top notch of reported Ni-based OER catalysts (Table S5 in Supporting information). Kinetic analysis *via* Tafel slopes (Fig. 1B) further confirm the superiority of Fe-$NiSe_2$-15 %, exhibiting the lowest Tafel slope of 33.8 mV/dec, significantly lower than Fe-$NiSe_2$-20 % (33.9 mV/dec), Fe-$NiSe_2$-10 % (37.17 mV/dec), Fe-$NiSe_2$-5 % (44.8 mV/dec), and $NiSe_2$ (56.3 mV/dec). This indicates Fe doping optimally accelerates the rate-determining step of OER, likely by modulating the electronic structure of active sites.

To probe charge transfer dynamics, electrochemical impedance spectroscopy (EIS) was employed (Figs. S9B and C in Supporting information). Fe-$NiSe_2$-15 % exhibits the smallest semicircle diameter, corresponding to the lowest charge transfer resistance (R_{ct}), followed by Fe-$NiSe_2$-20 % < Fe-$NiSe_2$-10 % < Fe-$NiSe_2$-5 % < $NiSe_2$ < RuO_2 (Table S4in Supporting information). This trend aligns well with the activity sequence, suggesting enhanced interfacial electron transfer kinetics in Fe-$NiSe_2$-15 %.

Intrinsic activity was quantified by normalizing the current density to both electrochemical specific surface area (ECSA) and catalyst mass. ECSA was estimated *via* double layer capacitance (C_{dl}) measurements, performed by recording CVs in the non-faradic potential region at scan rates ranging from 10 mV/s to 100 mV/s

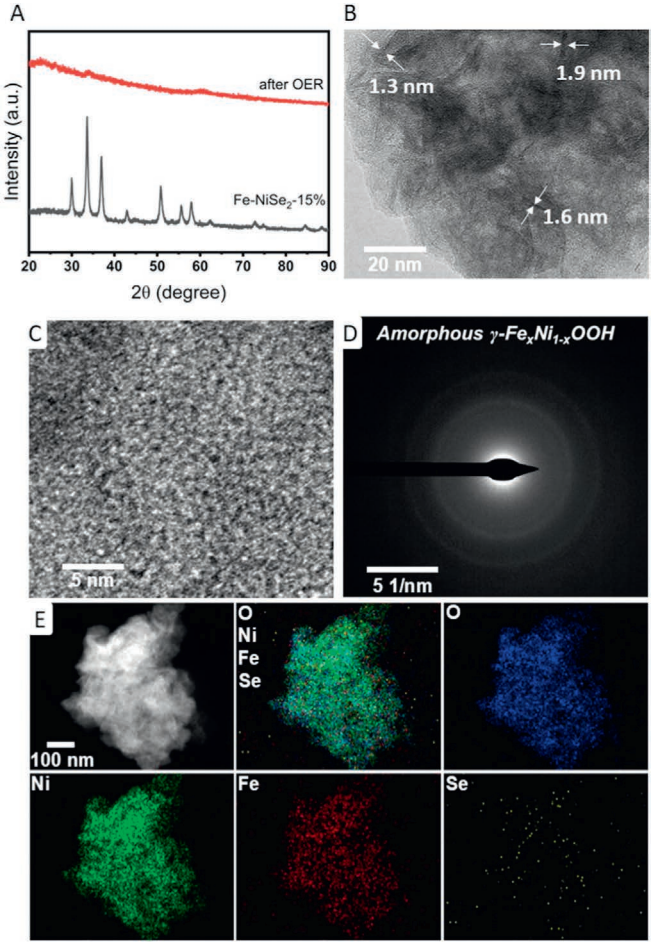


Fig. 2. Structure investigation of Fe-$NiSe_2$-15 % after CP at 100 mA/cm^2 for 24 h. (A) XRD patterns, (B) TEM image showing several thicknesses of nanosheets, (C) HR-TEM image, (D) selected area diffraction (SAED) pattern, (E) elemental mapping at a 100 nm scale by HAADF-STEM.

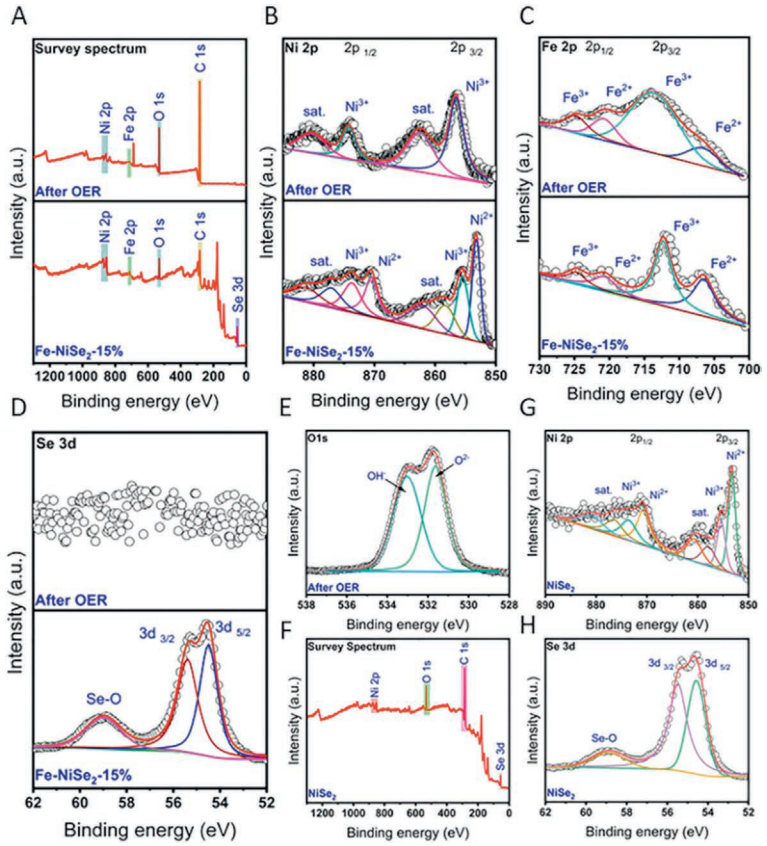


Fig. 3. XPS analysis before and after the chronopotentiometry (CP) test at 100 mA/cm^2 for 24 h. (A) The XPS survey spectrum. The high-resolution deconvoluted XPS spectra of (B) Ni 2p, (C) Fe 2p, (D) Se 3d, and (E) O 1s after the CP test. For comparison, the XPS data of $NiSe_2$ are also shown, including (F) the survey spectrum and the high-resolution deconvoluted spectra of (G) Ni 2p, (H) Se 3d.

(Fig. S10 in Supporting information). As shown in Fig. S10 and S9D (Supporting information), Fe-$NiSe_2$-15 % and Fe-$NiSe_2$-20 % exhibit the highest C_{dl} value of 1.17 mF/cm^2, compared to Fe-$NiSe_2$-10 % (1.05 mF/cm^2), Fe-$NiSe_2$-5 % (0.85 mF/cm^2), and pristine $NiSe_2$ (0.73 mF/cm^2). This trend suggests that Fe doping at 15 % optimally increases the electrochemically active surface area, exposing more accessible sites for OER. Normalized LSV curves (Fig. 1C) confirm Fe-$NiSe_2$-15 % achieves the highest specific activity (4 mA/cm$_{ECSA}^2$ at 1.43 V *vs.* RHE), while mass activity reaches 300 A/g at η = 230 mV- 61-fold higher than commercial RuO_2, also outperforming other counterparts (Fig. 1D and Fig. S9E in Supporting information). Furthermore, turnover frequency (TOF) calculations at η = 210 mV yield 0.1 s^{-1} for Fe-$NiSe_2$-15 %, surpassing Fe-$NiSe_2$-20 % (0.07 s^{-1}), Fe-$NiSe_2$-10 % (0.06 s^{-1}), Fe-$NiSe_2$-5 % (0.041 s^{-1}), and $NiSe_2$ (0.019 s^{-1}) (Fig. 1E and Fig. S9F in Supporting information). The numbers of active sites were calculated based on the integration of reduction peaks in Fig. S11 (Supporting information). This multi-metric superiority confirms Fe-$NiSe_2$-15 % as the most intrinsically active catalyst in the series. Additionally, the long-term stability was assessed *via* chronopotentiometry (CP) at 100 mA/cm^2 (Fig. 1F). Fe-$NiSe_2$-15 % maintains 90 % initial activity after 300 h, demonstrating exceptional durability under harsh OER conditions. More importantly, the alkali water electrolyzer of Pt‖Fe-$NiSe_2$-15 % requires only 1.48 V to reach current density of 20 mA/cm^2, outperforming that of Pt/C‖RuO_2 (1.65 V). Moreover, it can work stably for more than 80 h without significant voltage decay at 100 mA/cm^2 (Fig. S12 in Supporting information), indicating the potential industrial application for water splitting.

To unravel the structural evolution and active site origin of Fe-$NiSe_2$-15 % during OER, post-test characterizations were performed after 24 h chronopotentiometry at 100 mA/cm^2. XRD pattern (Fig. 2A) reveals broadened diffraction features with diminished intensity, indicative of complete amorphization. Morphological evolution was captured by electron microscopy: precatalyst nanoparticles (Figs. S2 and S3) reconstructed into ultrathin nanosheets (Fig. S13 in Supporting information and Fig. 2B) with lateral thickness <2 nm as evidenced by Atomic Force Microscopy images (AFM, Fig. S14 in Supporting information). High resolution TEM (HR-TEM) image confirms the dominantly amorphous nature of these nanosheets (Fig. 2C), evidenced by the absence of lattice fringes, while selected-area electron diffraction (SAED, Fig. 2D) displays diffuse halos without discrete spots, ruling out residual crystalline phases. Elemental redistribution during reconstruction was quantified through nanoscale EDX mapping (Fig. 2E): Selenium content drops by over 99 % (from 63.68 at% for Fe-$NiSe_2$-15 % to 0.2 at% after activation to 0.15 at% after CP test), replaced by oxygen incorporation (52.09 at%) to form γ-$Fe_xNi_{1-x}OOH$ (Tables S2 and S3 in Supporting information). Notably, Fe and Ni maintain homogeneous distribution with atomic Fe/Ni ratio preserved at 0.09 (*vs.* initial 0.085), confirming structural integrity despite drastic phase transformation at the activation process (Table S3 in Supporting information). This synergistic amorphous 2D architecture-combining metastable oxyhydroxide chemistry with maximized surface accessibility-establishes the fundamental structure-correlation underlying the exceptional OER performance.

Comprehensive XPS analysis elucidates the dynamic chemical evolution of Fe-$NiSe_2$-15 % during prolonged OER operation. Calibration of the binding energies was first done using C 1s (284.8 eV). The initial survey spectra (Fig. 3A) confirm the coexistence of Ni, Fe, Se, and trace surface oxygen species, with a distinct Se 3d peak (54.47 eV) verifying successful selenium incorporation.

Post-OER characterization reveals complete disappearance of Se 3d signals (<0.5 at% detection limit) alongside a dramatic increase in O 1s intensity, consistent with full structural reconstruction toward oxyhydroxide phases. High-resolution Ni 2p spectra (Fig. 3B) identify critical oxidation state transitions: Pristine catalyst surface exhibits mixed Ni^{2+} (853.21 eV) and Ni^{3+} (855.43 eV) states, accompanied by satellite peaks characteristic of Ni-Se bonding (857.84/861.13 eV). Following 24 h OER operation, sharp Ni^{3+} (856.6 eV) with a +1.17 eV binding energy shift relative to initial Ni^{3+} states, matching reference spectra for γ-NiOOH phases [16,17]. The complete absence of Ni^{2+} signals confirms irreversible complete surface oxidation to catalytically active Ni^{3+} species.

Parallel Fe 2p XPS analysis (Fig. 3C) reveals retained iron incorporation with modified oxidation states: Initial Fe^{2+} (39.2 %) and Fe^{3+} (60.8 %) components transition to predominantly Fe^{3+} (76.8 %) post OER test, indicating progressive Fe oxidation [18]. Se 3d spectrum (Fig. 3D) transitions from metallic Se (54.47/55.38 eV) and surface SeO_2 (58.97 eV) [19,20] to complete signal loss post-OER, which confirms near-total Se leaching. Oxygen speciation further supports structural reconstruction, with O 1s peaks (Fig. 3E) resolving into lattice oxygens (531.6 eV) and surface hydroxyl groups (533.0 eV)-diagnostic of γ-NiOOH phase [21]. The surface of $NiSe_2$ was also investigated by XPS spectra, showing the surface oxidation of Ni and Se species (Figs. 3F-H). These correlative analyses demonstrate Fe doping accelerates a three-stage reconstruction pathway: (1) Initial selenium oxidation (Se^{-2} to SeO_2) and dissolution, (2) progressive nickel oxidation (Ni^{2+} to Ni^{3+}) coupled with iron redox modulation, and (3) final stabilization into amorphous γ-$Fe_xNi_{1-x}OOH$ nanosheets. This structural evolution generates defect-rich architectures with optimized Ni^{3+}-O-Fe^{3+} active motifs, rationalizing the exceptional OER performance through enhanced active site exposure and optimized electronic configurations.

To dynamically track the structural evolution of Fe-$NiSe_2$-15 % during OER process, we employed cryo-quenched *operando* Raman spectroscopy. Catalysts were rapidly frozen using liquid N_2 after 24 h OER operation at 100 mA/cm^2, effectively preserving metastable intermediates. While pristine $NiSe_2$ and Fe-$NiSe_2$-15 % powder showed featureless Raman spectra between 400 cm^{-1} and 700 cm^{-1} (Figs. 4A and B), the post-OER samples exhibited two definitive Raman vibrational modes: A depolarized bending mode at 480 cm^{-1} ($\delta(Ni^{III}\text{-}O)$) and a polarized stretching mode at 560 cm^{-1} ($\nu(Ni^{III}\text{-}O)$), characteristic of γ-NiOOH phases [22]. This spectroscopic evidence conclusively establishes the electro-chemical reconstruction of Fe-$NiSe_2$ into γ-$Fe_xNi_{1-x}OOH$ under operational conditions, corroborating our XPS observations of nickel oxidation and selenium depletion.

Potential-dependent Raman spectroscopy (Figs. 4C and D) further resolved the mechanistic sequence: Below 1.35 V *vs.* RHE, Fe^{3+} sites preferentially stabilize O-O^- intermediates through strong orbital hybridization (Fe 3d-O 2p), lowering the energy barrier for O-O bond formation. As potentials exceed 1.45 V, intensification of the 560 cm^{-1} Ni^{III}-O vibration with O_2 bubble evolution, indicating Ni^{3+} centers drive the final O-O^- disproportionation through enhanced electron withdrawal from anti-bonding orbitals.

First-principles calculations quantify this dual-site synergy: The Fe-incorporated γ-phase demonstrates a 18 % reduction in O-O^- formation energy (1.36 *vs.* 1.54 eV for Ni-only sites, Fig. 4E), while the overall reaction pathway identifies $^*O \rightarrow {}^*OOH$ as the potential-determining step with an overpotential of 0.48 V (Fig. 4F). Crucially, metastable O-O^- bridges (detected at 1080 cm^{-1} in *operando* spectra) facilitates electron delocalization across Fe-O-Ni centers, simultaneously elevating Ni valence state and weakening $^*O$ adsorption energy barrier by 0.32 eV through dipole-charge interactions. Bader charge and OER reaction intermediates of γ-NiOOH and γ-$Fe_xNi_{1-x}OOH$-15 % are clarified in Fig. S15 (Supporting information).

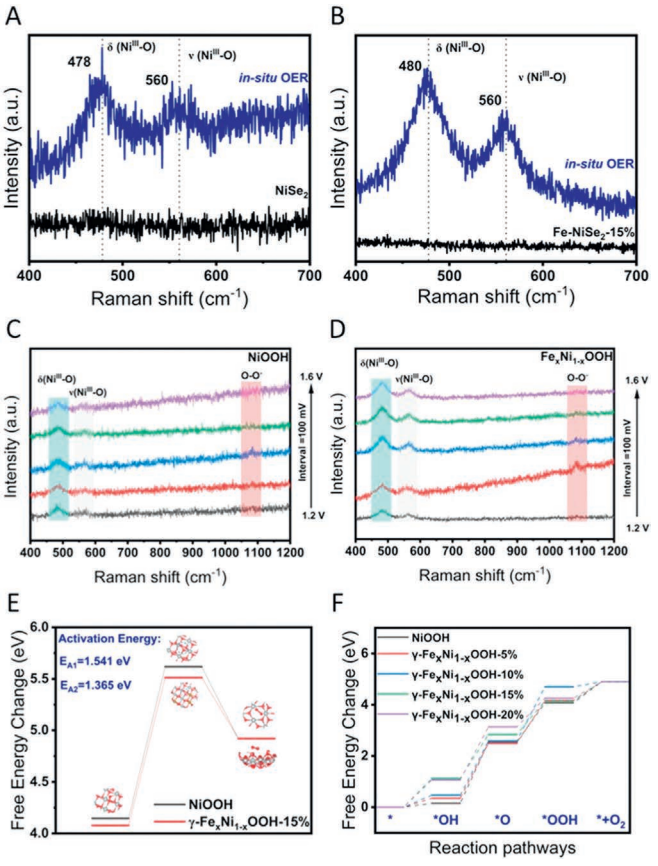


Fig. 4. Analysis of surface adsorption on catalysts. (A, B) Raman spectra of the as-prepared $NiSe_2$ and Fe-$NiSe_2$-15 % powder and after OER chronopotentiometry for 24 h at 100 mA/cm^2 (*in situ*) in 1 mol/L KOH. (C, D) *In situ* Raman spectra of OER process on (C) NiOOH and (D) $Fe_xNi_{1-x}OOH$ at different applied potentials in 1 mol/L KOH. (E) Transition state and activation energy during the adsorption of OOH to O_2 by NiOOH and $Fe_xNi_{1-x}OOH$-15 %. (F) Step diagram of the OER reaction mechanism.

This self-optimizing architecture-combining Fe-mediated O-O^- generation with Ni^{3+}-driven O_2 release-establishes a mechanistic bridge between our observed structural evolution (amorphous γ-phase formation) and exceptional catalytic performance. The synergistic redox interplay rationalizes both the 61-fold mass activity enhancement over RuO_2 and the sustained 300 h stability through continuous surface renewal.

In summary, this study demonstrates a facile low-temperature synthesis of Fe doped $NiSe_2$ as a high-efficiency pre-catalyst for alkaline oxygen evolution. Through *operando* characterization and post-test analysis, we unveil dynamic electrochemical reconstruction mechanisms: The initial crystalline Fe-$NiSe_2$ undergoes complete structural metamorphosis under activation process of cyclic voltammetry, evolving into ultrathin amorphous γ-$Fe_xNi_{1-x}OOH$ nanosheets *via* three synchronized processes: (1) Near-total selenium leaching (>99 % Se depletion), (2) progressive nickel oxidation ($Ni^{2+} \rightarrow Ni^{3+}$), and (3) iron-regulated morphological reorganization into 2D architectures. This self-engineered active phase delivers exceptional catalytic performance (overpotential $\eta_{20} = 163$ mV, stability >300 h at 100 mA/cm^2), attributable to three interconnected advantages: First, the amorphous γ-phase creates defect-rich surfaces exposing optimized Ni^{3+}-O-Fe^{3+} dual-active motifs that lower O-O bond formation barriers. Second, the ultrathin 2D morphology maximizes electrochemical interfaces. Third, Fe incorporation modulates charge distribution across Ni-O-

Fe centers, enhancing both electron transfer kinetics and structural resilience against oxidative corrosion.

Remarkably, this *in situ* electrochemical reconstruction strategy bypasses traditional complex catalyst design, establishing a general paradigm where transition metal chalcogenides serve as dynamic precursors that self-optimize into high-performance oxyhydroxides under operational conditions. The fundamental insights into reconstruction-driven activation mechanisms open new avenues for developing adaptive electrocatalysts tailored for industrial water splitting applications.

Declaration of competing interest

The authors declare that they have no known competing financial interests or personal relationships that could have appeared to influence the work reported in this paper.

CRediT authorship contribution statement

Elhussein Desoki Helal: Writing – review & editing, Writing – original draft, Visualization, Validation, Software, Project administration, Methodology, Investigation, Formal analysis, Data curation, Conceptualization. **Wenhai Xu:** Writing – review & editing, Writing – original draft, Visualization, Validation, Software, Methodology, Investigation, Formal analysis, Data curation, Conceptualization. **Liyao Gao:** Formal analysis, Data curation. **Yizhe Li:** Formal analysis, Data curation. **Hao Sun:** Formal analysis, Data curation. **Qingzhen Xu:** Formal analysis, Data curation. **Imran Ali Chandio:** Formal analysis, Data curation. **Safdar Abbas:** Formal analysis, Data curation. **Abdul Hameed Pato:** Formal analysis, Data curation. **Mohamed Mokhtar Mohamed:** Formal analysis, Data curation. **Man Zhao:** Formal analysis, Data curation. **Wen Liu:** Supervision, Resources, Project administration, Funding acquisition.

Acknowledgments

The work was supported by the National Natural Science Foundation of China (Nos. 21771018 and 21875004), Beijing Natural Science Foundation and Xiaomi Joint Grants (No. L223011), and the Beijing University of Chemical Technology (No. buctrc201901).

Supplementary materials

Supplementary material associated with this article can be found, in the online version, at doi:10.1016/j.cclet.2025.111311.

References

[1] J.H. Montoya, L.C. Seitz, P. Chakthranont, et al., Nat. Mater. 16 (2017) 70–81.
[2] L.L. Ma, Y.R. Hao, J. Sun, et al., Adv. Funct. Mater. 35 (2025) 2409924.
[3] J.X. Wen, Y.R. Hao, J. Sun, et al., Adv. Energy Mater. 15 (2025) 2405555.
[4] Z. Zhao, P.S. Lamoureux, A. Kulkarni, M. Bajdich, ChemCatChem 11 (2019) 3423–3431.
[5] L. Trotochaud, J.K. Ranney, K.N. Williams, S.W. Boettcher, J. Am. Chem. Soc. 134 (2012) 17253–17261.
[6] S. Lee, Y.C. Chu, L. Bai, H.M. Chen, X. Hu, Chem. Catal. 3 (2023) 100475.
[7] J. Masa, W. Schuhmann, ChemCatChem 11 (2019) 5842–5854.
[8] B.R. Wygant, K. Kawashima, C.B. Mullins, ACS Energy Lett. 3 (2018) 2956–2966.
[9] X. Li, G.Q. Han, Y.R. Liu, et al., ACS Appl. Mater. Interfaces 8 (2016) 20057–20066.
[10] S. Ghosh, B. Dasgupta, S. Kalra, et al., Small 19 (2023) 2206679.
[11] B. Dasgupta, J.N. Hausmann, R. Beltrán-Suito, et al., Small 19 (2023) 2301258.
[12] K. Ye, Y. Zhang, S. Mourdikoudis, et al., Small 19 (2023) 2302341.
[13] X. Chia, M. Pumera, Nat. Catal. 1 (2018) 909–921.
[14] J. Yu, G. Cheng, W. Luo, Nano Res. 11 (2018) 2149–2158.
[15] P. Wei, J. Li, H. Kang, et al., Int. J. Energy Res. 44 (2020) 845–854.
[16] C.-W. Hu, Y. Yamada, K. Yoshimura, J. Mater. Chem. C 4 (2016) 5390–5397.
[17] Z. Yan, H. Sun, X. Chen, et al., Nat. Commun. 9 (2018) 2373.
[18] M. Gong, Y. Li, H. Wang, et al., J. Am. Chem. Soc. 135 (2013) 8452–8455.
[19] C. Xia, Q. Jiang, C. Zhao, M.N. Hedhili, H.N. Alshareef, Adv. Mater. 28 (2015) 77.
[20] S. Huang, Q. He, W. Chen, et al., Chem. Eur. J. 21 (2015) 4085–4091.
[21] E.L. Ratcliff, J. Meyer, K.X. Steirer, et al., Chem. Mater. 23 (2011) 4988–5000.
[22] A.C. Garcia, T. Touzalin, C. Nieuwland, N. Perini, M.T. Koper, Angew. Chem. Int. Ed. 58 (2019) 12999–13003.